

# Geometry of singular structures in magnetohydrodynamic flows

Rainer Grauer and Christiane Marliani

*Institut für Theoretische Physik I, Heinrich-Heine-Universität Düsseldorf, D-40225 Düsseldorf, Germany*

(Received 22 August 1997; accepted 3 April 1998)

The flattening of current sheets is investigated by means of numerical simulations of the ideal incompressible magnetohydrodynamic equations in two dimensions. The use of adaptive mesh refinement techniques allows one to resolve the more and more singular structures and to follow the exponential growth of current density. The numerical results are in good agreement with a scaling ansatz proposed by Sulem *et al.* [J. Plasma Phys. **33**, 191 (1985)]. The geometry of the current sheets is characterized by the alignment properties of the deformation matrices. © 1998 American Institute of Physics. [S1070-664X(98)01707-8]

## I. INTRODUCTION

The formation of singular structures in hydro- and magnetohydrodynamic flows is not only interesting on its own, but may also shed some light on the problem of intermittency. The effect of intermittency shows up, e.g., in the anomalous (nonlinear) behavior of the scaling exponents for high order structure functions. How singularities of different strength are related to the scaling exponents is described in Frisch and Parisi<sup>1</sup> and the connection of how the geometry of the singular structures enters in a phenomenological model for structure functions was made by She and Leveque.<sup>2</sup> This model can be generalized to a model with two parameters, which are determined by the scaling of the most dissipative features and the codimension of the intermittent structures.<sup>3,4</sup> The She–Leveque phenomenology was successfully applied to magnetohydrodynamic systems<sup>5,6</sup> and shows surprisingly good agreement with experimental data. However, recent hydrodynamic experiments and numerical simulations show different scaling exponents for longitudinal and transversal structure functions.<sup>7–9</sup> Since the phenomenological model does not distinguish between them, it becomes clear that some ingredients of this model are not yet understood.

Another motivation for studying singular structures is due to the instanton approach.<sup>10,11</sup> The instanton solution for the probability density of the negative velocity gradients was calculated by Balkowsky *et al.*<sup>11</sup> in the case of the Burgers equation. There the main contribution in the path integral originates from a singularity which is closely related to the singularity (shock) of the inviscid equation.

In addition, it should be mentioned that no analytical estimates for the growth of current density and vorticity are available at present even in the two-dimensional case. The knowledge is slightly more advanced for the three-dimensional Euler equations, where it was shown by Constantin *et al.*<sup>12</sup> that the growth of vorticity is controlled by the smoothness of its direction. A statement like this for ideal magnetohydrodynamic flows is still missing, but likely to hold. Therefore, a careful analysis of the geometric properties of current sheets is a first step in this direction.

In this paper, we study the ideal incompressible magnetohydrodynamic (MHD) equations in two dimensions for the

velocity  $\mathbf{u}$  and the magnetic field  $\mathbf{B}$ . Sum and difference of the dynamic equations have a more symmetric form, namely,

$$\partial_t \mathbf{z}^\pm + \mathbf{z}^\mp \cdot \nabla \mathbf{z}^\pm = -\nabla p, \quad \nabla \cdot \mathbf{z}^\pm = 0 \quad (1)$$

with the Elsässer fields  $\mathbf{z}^\pm = \mathbf{u} \pm \mathbf{B}$  and the pressure  $p$ , which is the sum of fluid and magnetic pressure. In two dimensions, using the divergence freedom of velocity and magnetic field, it is possible to formulate the dynamic equations for scalar quantities. Taking the  $z$  component of the curl of the above equations yields

$$\partial_t \omega^\pm + \mathbf{z}^\mp \cdot \nabla \omega^\pm = \mathbf{e}_z \cdot \sum_i \nabla z_i^\pm \times \nabla z_i^\mp \quad (2)$$

with  $\omega^\pm = [\nabla \times \mathbf{z}^\pm]_z$  meaning the sum and difference of vorticity  $\omega$  and current density  $j$  and with  $z_i^\pm$  the  $i$ th component of the vector  $\mathbf{z}^\pm$  (see Pouquet<sup>13</sup>). The vorticities  $\omega^\pm$  are related to the flux functions by  $\Delta \psi^\pm = \omega^\pm$ . The divergence free vector fields can be obtained as  $\mathbf{z}^\pm = \mathbf{e}_z \times \nabla \psi^\pm$ .

These equations (1) are numerically solved using adaptive mesh refinement, which is described in more detail in the next section. The numerically obtained solutions are compared with a simple scaling ansatz and confirm the analysis of Sulem *et al.*<sup>14</sup> The observed exponential growth of current density and vorticity is explained by a depletion of the nonlinear production term  $\mathbf{e}_z \cdot \sum_i \nabla z_i^\pm \times \nabla z_i^\mp$  as described in Sec. III.

## II. ADAPTIVE MESH REFINEMENT FOR SINGULAR STRUCTURES

The idea of adaptive mesh refinement is near at hand. Starting with one grid of a given resolution (in most cases we chose  $256 \times 256$  mesh points) the partial differential equation is solved with some appropriate scheme which will be described below. After a certain number of time steps it is checked whether the local numerical resolution is still sufficient on the whole grid. If one detects that locally finer grids are needed, a first refinement is carried out. For that, critical points, i.e., those locations where the error of the discretization exceeds a given value, are marked on the grid. In addition to these grid points adjacent ones are included. The size of this neighborhood is determined by the local velocities

and the time interval to the next regridding. In this way it is avoided that the grid hierarchy fails to follow a moving structure. Now, the marked points have to be covered with rectangular grids of finer resolution as efficiently as possible. Our algorithm for this purpose is very similar to the one by Berger and Colella<sup>15</sup> and was recently described in Friedel *et al.*<sup>16</sup> On the grids of the newly-built level, the spatial discretization length and the time step are reduced by a factor  $r$ , which is called the refinement factor. The new grids are filled with data by interpolation from the preceding level. On both levels integration advances until the resolution again becomes locally insufficient. The rebuilding of the grid hierarchy, starting with the actual level and proceeding on all subsequent levels, begins when the above-mentioned threshold for the error is locally exceeded, e.g., if the current sheet has moved out of the region covered with finer grids or if local gradients have developed such that the prescribed accuracy is not guaranteed. Next, the critical points are collected on all grids of each level. On the basis of the resulting lists of critical points new grids are generated. Before they can be filled with data, it has to be checked whether they are correctly embedded in grids of the preceding level. If data existed on grids of the same level before the regridding, these have to be taken instead of the interpolated data.

Having explained the strategy of adaptive mesh refinement, it remains for us to comment on the integration scheme that is used on all grids involved. It is a projection method combined with second order upwinding, motivated by the work of Bell *et al.*<sup>17,18</sup> The same scheme, but with dissipative terms included, has already been used for nonadaptive simulations of the MHD equations.<sup>19</sup>

At the beginning of the recursive integration, the grids of the actual,  $n$ th level are all advanced to a time  $t_0$ . On each grid of this level a time step is carried out. Afterwards we have the fields  $\omega^\pm$  at the time  $t_0 + dt$ . The grid hierarchy is organized such that each of the disjunct rectangles has the additional boundary data needed for the evaluation of finite differences. These data are supplied by spatial and temporal interpolation from the preceding level. Where possible, data from neighboring grids are used instead. Then on each grid the Poisson equations  $\omega^\pm = \Delta \psi^\pm$  with fixed boundary conditions are solved. Neighboring grids have overlapping boundaries. The difference of the solution of the Poisson equation on neighboring grids is reduced by additive Schwarz iteration until its value is below a given threshold. Afterwards we have to carry out  $r$  time steps of size  $dt/r$  on the  $n+1$ th level's grids. The recursion ends when all data of the  $n$ th and the subsequent levels are advanced to the time  $t_0 + dt$  and data of the coarser grids are improved by those from finer ones.

In the simulations described here, we apply periodic boundary conditions on the zeroth level. Of course, we have to ensure periodicity on the refined grids, too. Therefore grids bordering on the outer boundary have to exchange boundary values not only with their direct neighbors but also with periodic neighbors, i.e., those grids on the other side of the integration domain's outer boundary.

A parallelization of the adaptive mesh refinement code on shared memory machines is easily achieved and has been

implemented with Posix threads. The loops over grids are parallelized by passing the grids to different processors. As in our case, the number of grids on the finer levels has always been much higher than the number of available processors such that an efficient distribution of the computational effort does not pose any problems.

To gain insight into the physical properties, it is necessary to evaluate several local and integral quantities based on the data distributed over all grids in the hierarchical structure. Local quantities are easily determined in a loop over all levels' grids. In order to obtain integrated quantities, on each level one first has to sum up the contributions from those parts that are not covered by grids of the subsequent finer level. Afterwards the integral on the whole domain is found as the sum over all levels.

### III. NUMERICAL RESULTS AND GEOMETRY OF CURRENT SHEETS

The two-dimensional incompressible magnetohydrodynamic equations are solved in a quadratic box of size  $L = 2\pi$  applying periodic boundary conditions. We study two different types of initial conditions. The first is the well-known Orszag–Tang vortex

$$\varphi^0(x, y) = 2(\cos(x) + \cos(y)),$$

$$\psi^0(x, y) = 2 \cos(2x) + \cos(2y),$$

where  $\varphi$  and  $\psi$  are the kinetic and magnetic flux functions. It was studied in numerical simulations by Frisch *et al.*<sup>20</sup> The second type of initial conditions is similar to those, but made less symmetric by introducing arbitrary phase shifts. Actually, we choose

$$\varphi^0(x, y) = \cos(x + 1.4) + \cos(y + 2.0),$$

$$\psi^0(x, y) = \frac{1}{3}(\cos(2x + 2.3) + \cos(y + 6.2)).$$

These initial conditions are obtained by translation in the  $y$  direction by a value of  $-1.5$  from those introduced by Biskamp and Welter<sup>21</sup> for simulations of turbulent magnetohydrodynamic flows, and in the following we will refer to them as Biskamp–Welter initial conditions.

Our numerical simulations start with a fixed grid of  $256^2$  grid points and while time advances several refinements with factor  $r=2$  are performed ending up with six levels for the Orszag–Tang initial conditions and seven in the Biskamp–Welter case. Therefore, at the end the finest level's resolution corresponds to  $16\,384^2$  or  $32\,768^2$  grid points on a fixed grid. The efficiency of adaptive mesh refinement for singular current sheets was recently discussed in Friedel *et al.*<sup>16</sup>

Contour plots of vorticity  $\omega$  and current density  $j$  illustrating the formation of current sheets starting with the Orszag–Tang vortex are shown in Figs. 1 and 2, while plots for the second set of initial conditions are given in Figs. 3 and 4. The covering with refined, nested grids is shown exemplarily for the vorticity in Fig. 1. For both initial conditions, sheet-like structures with decreasing thickness evolve. For the Orszag–Tang vortex a simple, highly symmetric sheet is found in the central region. There the current density has a thin elliptic structure and the vorticity shows a flat

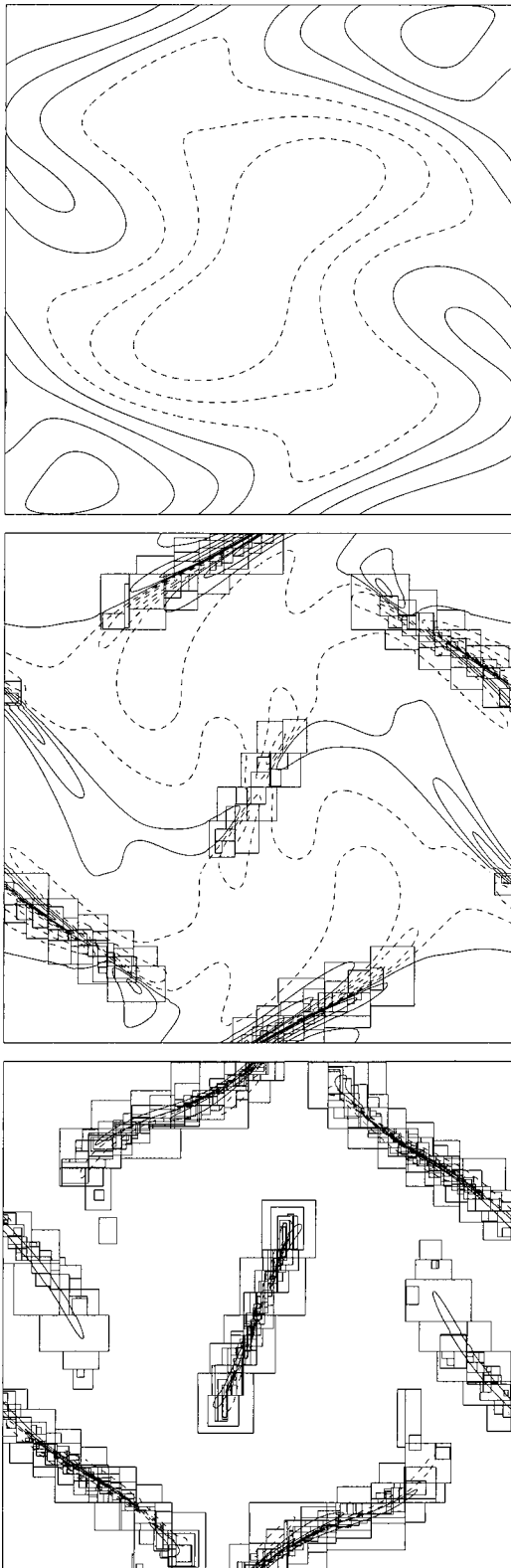


FIG. 1. Vorticity at times  $t=0.20, 0.62, 0.84$  for the simulation with Orszag–Tang initial conditions.

quadrupole-like configuration. In contrast, for the second initial conditions more complicated sheets appear.

During the evolution of thinner and thinner current sheets the absolute value of the current density at the local extrema increases exponentially. Following several of these

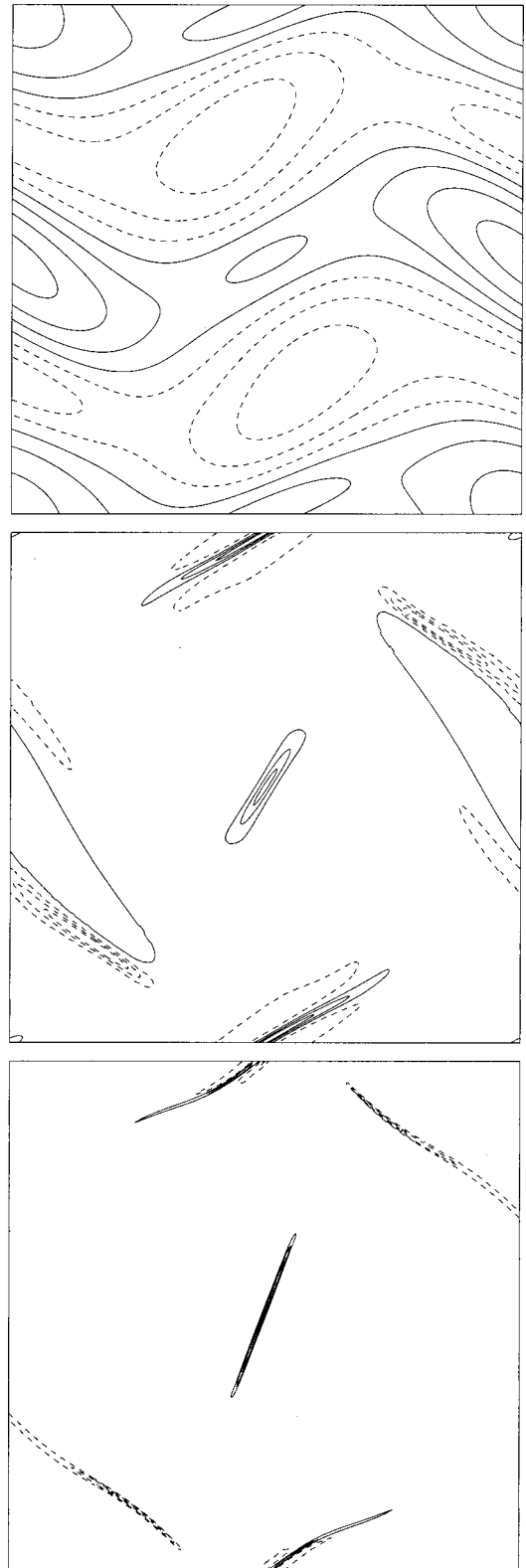


FIG. 2. Current density at times  $t=0.20, 0.62, 0.84$  for the simulation with Orszag–Tang initial conditions.

extreme values, one finds, after a transitional period where the sheets begin to form, that in all extrema the current density grows proportionally to  $\exp(at)$ , but with different values of  $a$ , since the growth of local current sheets depends on the energy of the surrounding flow field. Therefore, the magnetic

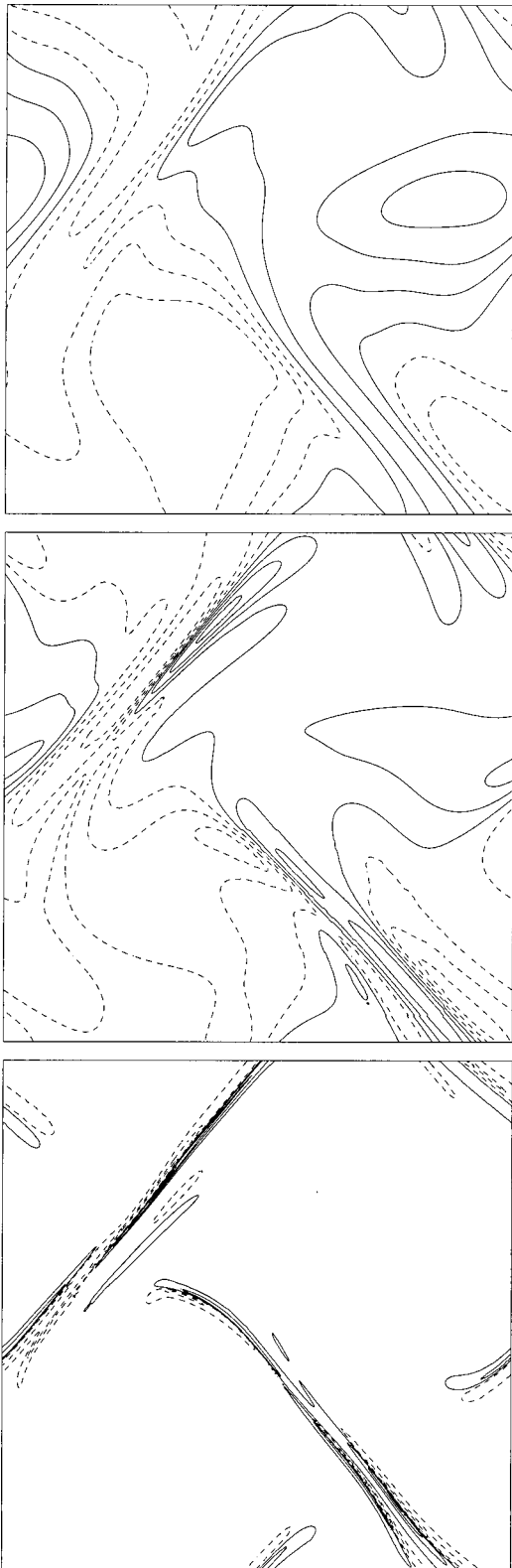


FIG. 3. Vorticity at times  $t=0.41, 1.57, 2.65$  for the simulation with Biskamp–Welter initial conditions.

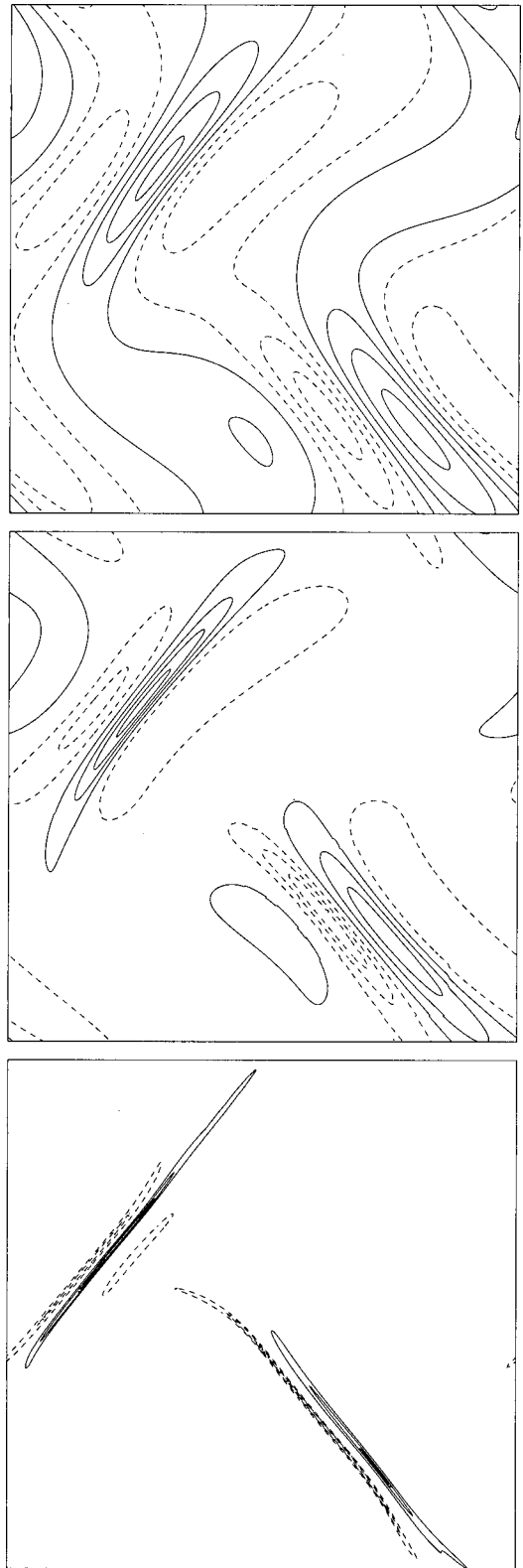


FIG. 4. Current density at times  $t=0.41, 1.57, 2.65$  for the simulation with Biskamp–Welter initial conditions.

enstrophy adds all contributions of the different current sheets possessing different values of  $a$  and consequently does itself not show a clear exponential behavior. At very late times, where the enstrophy integral is dominated by the strongest current sheet, a clear exponential growth can be

recovered. In addition, the extreme values of  $j$  are much larger than those of  $\omega$ , so that  $\omega^\pm$  are dominated by the current density. In Fig. 5 we give a semilogarithmic plot of the absolute values of the current density for the first initial conditions in the central minimum and the maxima in the

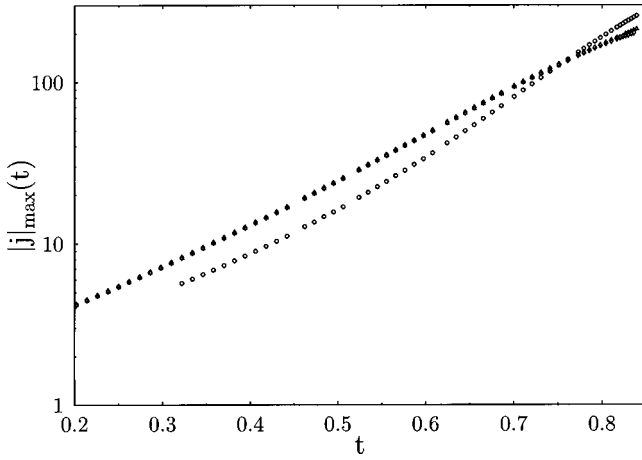


FIG. 5. Temporal evolution of the absolute value of the current density in its local extrema for the Orszag–Tang initial conditions.

upper right and the lower left region. An analogous picture is found in the case of Biskamp–Welter initial conditions as illustrated in Fig. 6, where the values for the maximum and minimum in the sheet structure in the lower right region are shown.

### A. Self-similarity and scaling ansatz

While the absolute values of current density in the extrema grow exponentially, the current sheets are getting thinner and thinner. This fact motivates a scaling ansatz as first proposed by Sulem *et al.*<sup>14</sup> for the region near neutral  $X$  points, i.e., points where the magnetic field vanishes and the magnetic flux function shows a hyperbolic topology. Let us briefly summarize their approach. They consider the dynamic equations for the  $x$  component of velocity  $\mathbf{u}$  and the magnetic flux function  $\psi$  in a coordinate system in the neighborhood of the  $X$  point with the  $x$  axis chosen along the current sheet and the  $y$  axis perpendicular. They can be written as

$$\partial_t \psi + u_x \partial_x \psi + u_y \partial_y \psi = 0,$$

$$\partial_t u_x + u_x \partial_x u_x + u_y \partial_y u_x = B_x \partial_x B_x + B_y \partial_y B_x - \partial_x p.$$

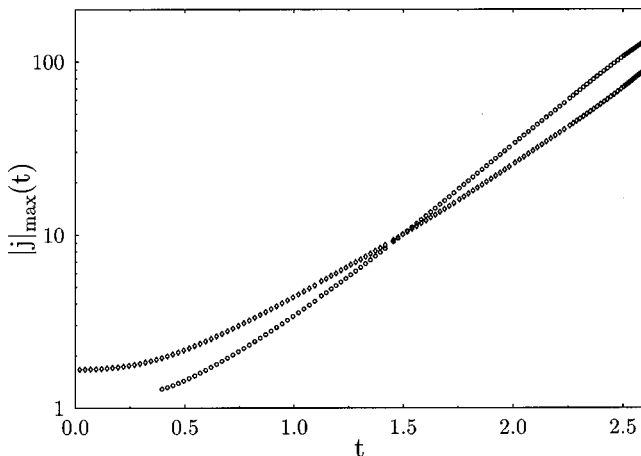


FIG. 6. Temporal evolution of the absolute value of the current density in its local extrema for the Biskamp–Welter initial conditions.

Formulating the scaling ansatz, one has to account for the observation that velocity and magnetic field remain of the same order of magnitude for all times. For the long time behavior, this leads to the following equations for the scaled variables which are denoted by tilded symbols:

$$\begin{aligned} \varphi(x, y, t) &= l(t) \tilde{\varphi}(\tilde{x}, \tilde{y}), \\ \psi(x, y, t) &= l(t) \tilde{\psi}(\tilde{x}, \tilde{y}), \\ p(x, y, t) &= l(t) \tilde{p}(\tilde{x}, \tilde{y}). \end{aligned} \quad (3)$$

The length scales  $L(t)$  and  $l(t)$  are defined by

$$\tilde{x} = \frac{x}{L(t)} \quad \text{and} \quad \tilde{y} = \frac{y}{l(t)}. \quad (4)$$

This ansatz is now plugged into the dynamic equations. Dividing by  $l(t)$ , one ends up with two equations of the form

$$\frac{\dot{l}(t)}{l(t)} f(\tilde{x}, \tilde{y}) + \frac{\dot{L}(t)}{L(t)} g(\tilde{x}, \tilde{y}) + \frac{1}{L(t)} h(\tilde{x}, \tilde{y}) = 0.$$

They consist of products of time and space dependent factors. There are several possibilities to fulfill both equations simultaneously. Among these relations for the length scales only one is consistent with a flattening sheet structure, namely

$$\frac{\dot{l}}{l} \sim \frac{1}{L}, \quad \left| \frac{\dot{L}}{L} \right| \ll \frac{1}{L}.$$

The length scale  $L(t)$  along the sheet becomes independent of time, whereas the perpendicular scale  $l(t)$  shows exponential behavior

$$l(t) = l(0) \exp(-\Lambda t/L).$$

The factor  $\Lambda$  is assumed to be positive. That means an exponential decay of the sheet thickness is consistent with the dynamic equations. Inserting the determined temporal behavior of the scales  $L(t)$  and  $l(t)$  into the equations yields time-independent partial differential equations in the spatial variables  $\tilde{x}$  and  $\tilde{y}$ .

The development and growth of self-similar structures is also reflected by the behavior of certain integral quantities. This will now be shown by some integrals over first order derivatives of velocity and magnetic field

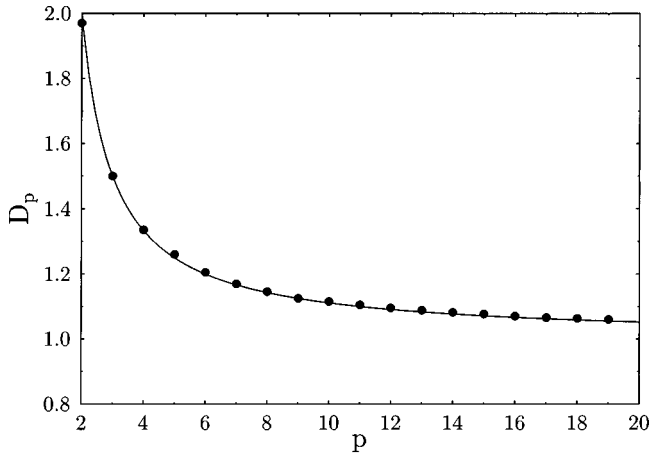
$$D_p = \int \int (|\partial_x u_x|^p + |\partial_y u_x|^p + \dots + |\partial_y B_y|^p) dx dy.$$

We expect that the integrals for higher order  $p$  are dominated by the contributions from the sheet structures where high values of some elements of the gradient matrices of velocity and magnetic field are found.

Assuming the scaling ansatz (3), (4) to hold for long periods, it follows that  $D_p$  behaves like  $l^{-(p-1)}$ . This yields a relation between the quantities of subsequent orders  $p$  and  $p+1$

$$D_{p+1} \sim l^{-p} \sim (D_p)^{p/(p-1)}.$$

To compare this prediction with numerical results, we evaluated the slope in doubly logarithmic plots of the time-dependent values of  $D_{p+1}$  as a function of those of  $D_p$  for

FIG. 7. Exponents of  $D_{p+1}(D_p)$  as a function of  $p$ .

each order  $p$ . The results for the run with Biskamp–Welter initial conditions are shown in Fig. 7. They are in good agreement with the curve representing the theoretical prediction. This result does not depend on the initial condition and the figure looks the same for the Orszag–Tang vortex initial conditions.

### B. Alignment properties of the deformation matrices

Let us start to discuss how the self-similarity is reflected by some local quantities which can be evaluated numerically. First, we calculated the eigenvalues of the deformation matrix of the magnetic field, i.e., the symmetric part of the gradient matrix with elements  $(\nabla \mathbf{B})_{i,j}^S = (\partial_i B_j + \partial_j B_i)/2$ . As the magnetic field is divergence free,  $\nabla \cdot \mathbf{B} = 0$ , it has pairs of eigenvalues with opposite sign,  $\lambda_1 = \lambda$  and  $\lambda_2 = -\lambda$ . Plugging the scaling ansatz into the equation for the gradient matrix of the magnetic field  $\mathbf{B}$  yields

$$\nabla \mathbf{B} = \begin{pmatrix} -\frac{1}{L} \partial_{\tilde{x}\tilde{y}} \tilde{\psi} & \frac{l}{L^2} \partial_{\tilde{x}\tilde{x}} \tilde{\psi} \\ -\frac{1}{l} \partial_{\tilde{y}\tilde{y}} \tilde{\psi} & \frac{1}{L} \partial_{\tilde{x}\tilde{y}} \tilde{\psi} \end{pmatrix}.$$

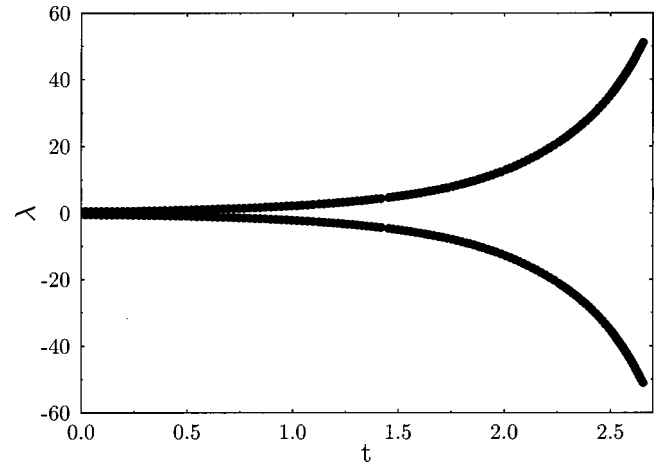
Using that the current density reads  $j = (l/L^2) \partial_{\tilde{x}\tilde{x}} \tilde{\psi} + (1/l) \partial_{\tilde{y}\tilde{y}} \tilde{\psi}$ , at late times the deformation matrix  $\nabla \mathbf{B}^S$  is dominated by the current density, resulting in

$$\nabla \mathbf{B}^S = \frac{1}{2} \begin{pmatrix} 0 & -j \\ -j & 0 \end{pmatrix}.$$

Therefore, the growth of the eigenvalue  $\lambda$  is given by  $\lambda = 1/2 |j|_{\max}$ .

In Fig. 8 we show the temporal evolution of the eigenvalues  $\lambda_1$  and  $\lambda_2$  for the simulation with Biskamp–Welter initial conditions. For the Orszag–Tang case the same behavior is found. To verify the relation  $\lambda = 1/2 |j|_{\max}$ , Fig. 9 shows a parametric plot of  $\lambda$  versus  $|j|_{\max}$  for the Orszag–Tang initial conditions. Excellent agreement with the prediction from the scaling ansatz is found even at early times.

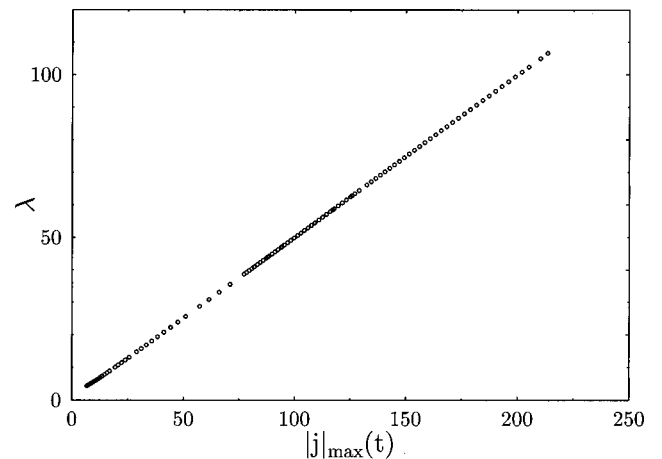
Now, we go one step further and investigate the eigenvectors of some deformation matrices. To each pair of eigen-

FIG. 8. Eigenvalues of the deformation matrix  $(\nabla \mathbf{B})^S$  as a function of time at the minimum of current density.

values  $\lambda_{1,2}$  corresponds a pair of orthogonal eigenvectors. We calculate the normalized eigenvectors of the deformation matrices of the Elsässer fields,  $(\nabla \mathbf{z}^\pm)^S$ , and study the dependence of the value of the current density on the angle between the eigenvectors  $\mathbf{E}_{1,2}^+$  of  $(\nabla \mathbf{z}^+)^S$  and  $\mathbf{E}_{1,2}^-$  of  $(\nabla \mathbf{z}^-)^S$  in a neighborhood of the current density's maximum. Results for the different initial conditions are shown in Figs. 10 and 11.

The angle between the eigenvectors referring to positive and negative eigenvalues of the two matrices approaches 90 or 0 deg where the current density has its extremal values. That means that locally the eigenvectors are approximately parallel or orthogonal. If this would be exactly valid, by transformation to this basis both deformation matrices become diagonal at the same time.

This behavior is consistent with the scaling ansatz as one can show by investigating the long time behavior of the eigenvectors. One finds that the deformation matrices  $(\nabla \mathbf{z}^\pm)^S$  asymptotically have the same set of eigenvectors, which take the form

FIG. 9. Parametric plot of the eigenvalue  $\lambda$  of the deformation matrix of  $\mathbf{B}$  versus the absolute value of the current density for the Orszag–Tang initial conditions.

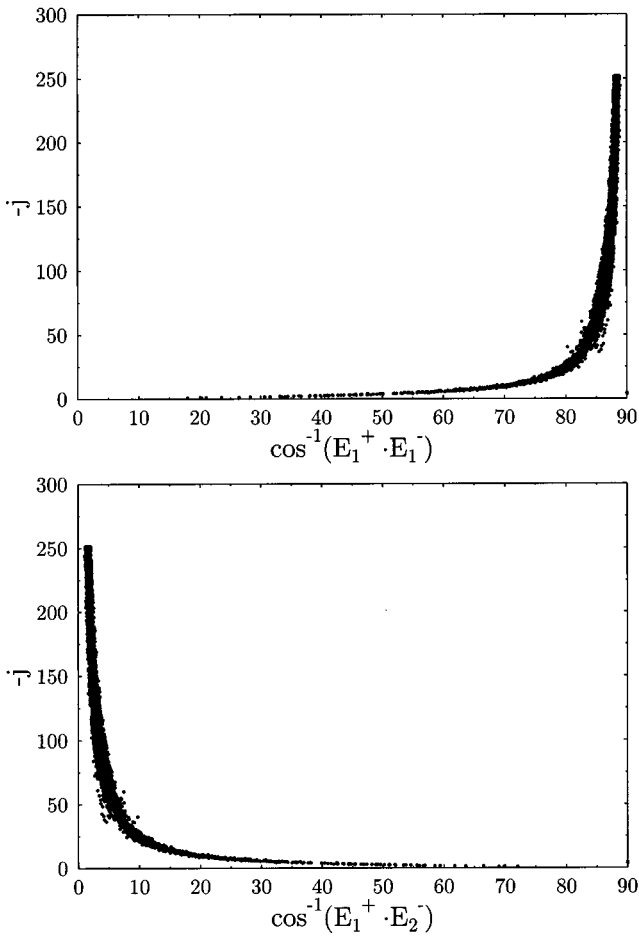


FIG. 10. Absolute value of current density as a function of the angle between the eigenvectors  $\mathbf{E}_1^+$  and  $\mathbf{E}_1^-$  (top) and  $\mathbf{E}_1^+$  and  $\mathbf{E}_2^-$  (bottom) at time  $t = 0.84$  in a neighborhood around  $\mathbf{x} = (3.09, 3.13)$ .

$$\mathbf{E}_1^\pm = \frac{1}{\sqrt{2}} \begin{pmatrix} -1 \\ \text{sign}(\omega^\pm) \end{pmatrix}, \quad \mathbf{E}_2^\pm = \frac{1}{\sqrt{2}} \begin{pmatrix} 1 \\ \text{sign}(\omega^\pm) \end{pmatrix}.$$

The properties of the gradient matrices of the Elsässer variables determine the nonlinear production term

$$\mathbf{e}_z \cdot \sum_i \nabla z_i^+ \times \nabla z_i^-$$

in the dynamic equations for the fields  $\omega^\pm$ . It should be noted that the influence of the production term was studied by Kinney *et al.*<sup>22</sup> in the context of a discrete vortex model and the contribution of the production term to the dissipative turbulent dynamics was studied in Ref. 23. The gradient matrices themselves can always be written as a sum of a symmetric matrix, namely, the traceless deformation matrix, and an antisymmetric matrix

$$(\nabla \mathbf{z}^\pm) = (\nabla \mathbf{z}^\pm)^S + \begin{pmatrix} 0 & -a^\pm \\ a^\pm & 0 \end{pmatrix}.$$

Now, we want to transform to the eigenvectors of  $\mathbf{E}_{1,2}^\pm$ . As can be seen from the formulas given above, in our case, where the Elsässer fields  $\omega^\pm$  are dominated by the current density, it follows that  $\mathbf{E}_1^+ = -\mathbf{E}_2^-$  and  $\mathbf{E}_2^+ = -\mathbf{E}_1^-$ . This leads to

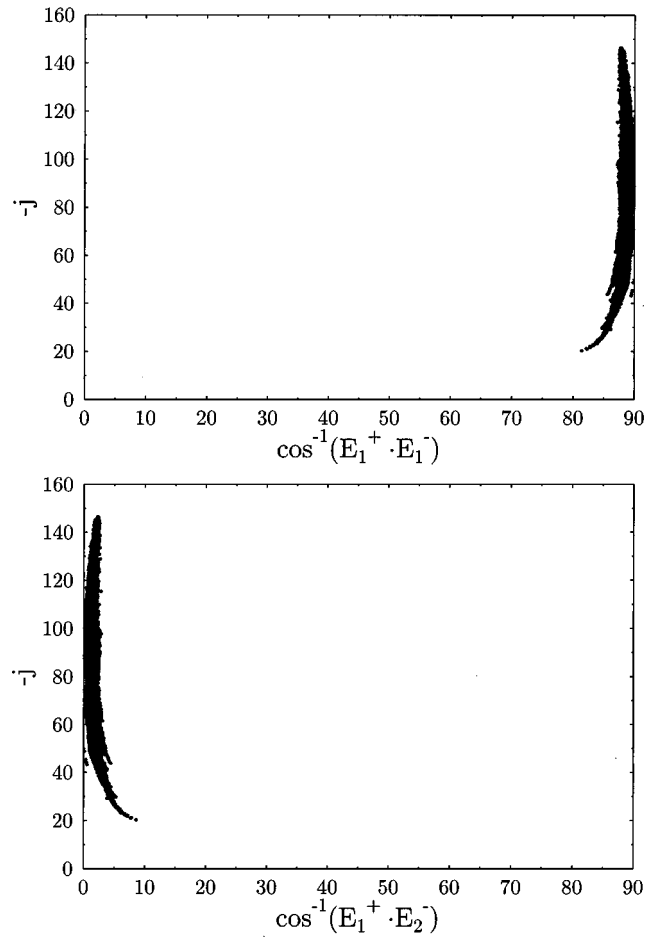


FIG. 11. Absolute value of current density as a function of the angle between the eigenvectors  $\mathbf{E}_1^+$  and  $\mathbf{E}_1^-$  (top) and  $\mathbf{E}_1^+$  and  $\mathbf{E}_2^-$  (bottom) at time  $t = 2.65$  in a neighborhood around  $\mathbf{x} = (1.06, 1.10)$ .

$$(\nabla \mathbf{z}^+) = \begin{pmatrix} \lambda^+ & -a^+ \\ a^+ & -\lambda^+ \end{pmatrix}$$

and similarly

$$(\nabla \mathbf{z}^-) = \begin{pmatrix} \lambda^- & a^- \\ -a^- & -\lambda^- \end{pmatrix}.$$

This result is now used to determine the behavior of the nonlinear production term. One finds that it cancels out, i.e., the nonlinearity is locally suppressed.

Looking at the upper plots in Figs. 10 and 11, one observes that the angle does not exactly equal 90 deg for high absolute values of the current density, but is slightly smaller. Let us briefly comment on the consequences for the gradient matrices and the nonlinear production term. As long as the eigenvectors of the two deformation matrices are not exactly the same, the transformation to the basis of eigenvectors of  $(\nabla \mathbf{z}^+)$  does only approximately diagonalize the other matrix  $(\nabla \mathbf{z}^-)$ . If these corrections of order  $\epsilon$  are taken into account in the calculation of the nonlinear production term, one ends up with a value proportional to  $\epsilon$  and the eigenvalue of the deformation matrix. This result is in agreement with the numerical evaluations as can be seen from Fig. 12, where we

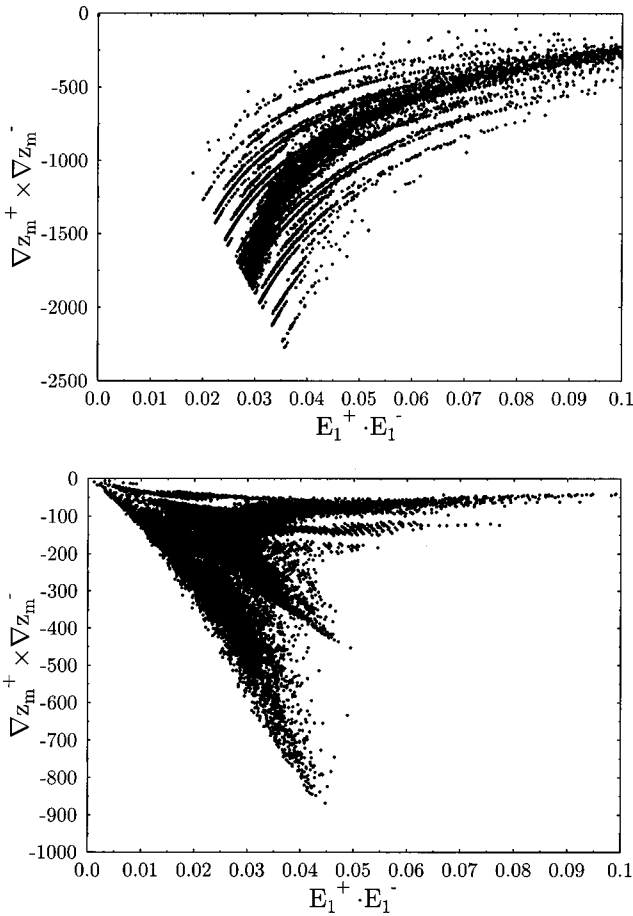


FIG. 12. Nonlinear production term as a function of the scalar product of the eigenvectors  $\mathbf{E}_1^+ \cdot \mathbf{E}_1^-$  (top) for the Orszag–Tang run at time  $t=0.84$  in the rectangle  $\mathbf{x} \in [3.09, 3.13]$ , (bottom) for the Biskamp–Welter run at time  $t=2.65$  in the rectangle  $\mathbf{x} \in [1.06, 1.10]$ .

show scatter plots of the nonlinear production term and the scalar product of eigenvectors  $\mathbf{E}_1^+ \cdot \mathbf{E}_1^-$  for both initial conditions.

The depletion of nonlinearity can also be seen in the  $L^p$  norms of the production term  $A^\pm = \mathbf{e}_z \cdot \sum_i \nabla z_i^\pm \times \nabla z_i^\mp$ . The temporal behavior of the  $L^p$  norms of the vorticities  $\omega^\pm$  follows from the dynamic equations (2). We multiply the equation for  $\omega^+$  by a factor  $(\omega^+)^{2n-1}$  and integrate over the domain. Partial integration with periodic boundary conditions and the divergence freedom of  $\mathbf{z}^\pm$  gives

$$\begin{aligned} \frac{d}{dt} \|\omega^+\|_{L^{2n}}^{2n} &= 2n \int A^+ (\omega^+)^{2n-1} d^2x \\ &\leq 2n \int |A^+| (\omega^+)^{2n-1} d^2x. \end{aligned}$$

On the right hand side, Young's inequality is applied to get

$$\frac{d}{dt} \|\omega^+\|_{L^{2n}}^{2n} \leq \|A^+\|_{L^{2n}}^{2n} + (2n-1) \|\omega^+\|_{L^{2n}}^{2n}.$$

Of course the analogous estimate for the  $L^{2n}$  norm of  $\omega^-$  is found by interchanging the indices “+” and “−.” Afterwards both results are added.

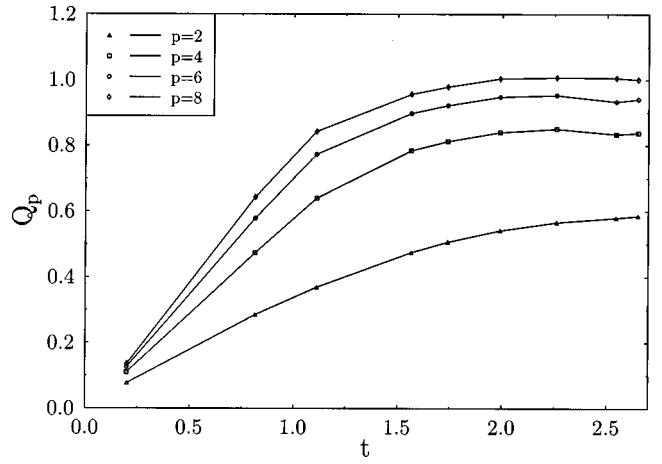


FIG. 13. Ratio  $Q_p$  for  $p=2,4,6,8$  as a function of time for Biskamp–Welter initial conditions.

At this point we want to make an assumption which is strongly supported by the numerical simulations. It says that the  $L^{2n}$  norms of the nonlinear production term  $A^+$  can be bounded by those of  $\omega^\pm$

$$\|A^+\|_{L^{2n}}^{2n} \leq \frac{C}{2} (\|\omega^+\|_{L^{2n}}^{2n} + \|\omega^-\|_{L^{2n}}^{2n}) \quad (5)$$

with a constant  $C$ . As  $A^- = -A^+$ , the same relation holds for the  $L^{2n}$  norms of  $A^-$ .

In Fig. 13 we show numerical values of the ratio

$$Q_p = \frac{\|A^+\|_{L^p}}{(\|\omega^+\|_{L^p}^p + \|\omega^-\|_{L^p}^p)^{1/p}}$$

for the values of  $p=2,4,6,8$  as functions of time. The results shown are taken from the run with Biskamp–Welter initial conditions. In the Orszag–Tang case they look qualitatively the same and are therefore not included here. After a transitional period where the sheets are developing the ratio  $Q_p$  approaches a constant value.

Figure 13 demonstrates nicely that the nonlinearity is depleted and the production term acts at most like a linear term. This is consistent with the observed exponential growth of  $\omega^-$ . More precisely, if we assume that (5) holds for any value  $2n$ , the time-derivative of  $\|\omega^+\|_{L^{2n}}^{2n} + \|\omega^-\|_{L^{2n}}^{2n}$  is bound in the following way:

$$\begin{aligned} \frac{d}{dt} (\|\omega^+\|_{L^{2n}}^{2n} + \|\omega^-\|_{L^{2n}}^{2n}) \\ \leq (C + 2n - 1) (\|\omega^+\|_{L^{2n}}^{2n} + \|\omega^-\|_{L^{2n}}^{2n}). \end{aligned}$$

Application of the Gronwall lemma yields that the sum of the  $2n$ th power of the  $L^{2n}$  norms does not grow faster than exponentially

$$\begin{aligned} \|\omega^+\|_{L^{2n}}^{2n} + \|\omega^-\|_{L^{2n}}^{2n} \\ \leq (\|\omega^+(0)\|_{L^{2n}}^{2n} + \|\omega^-(0)\|_{L^{2n}}^{2n}) \exp\{(C + 2n - 1)t\}. \end{aligned}$$

This result is also in perfect agreement with the scaling ansatz (3), (4). From this ansatz it follows immediately that



$Q_p = \text{const}$  as a result of cross differentiating with respect to  $x$  and  $y$  such that  $A^\pm$  scales like  $1/l$  which is the same as the scaling for  $\omega^\pm$ .

#### IV. CONCLUSIONS

In this paper, we showed that in the two-dimensional magnetohydrodynamic equations, the exponential growth of current density and vorticity is in accordance with a simple scaling ansatz. The necessary depletion of the nonlinear production term is demonstrated numerically. However, the question why the flow develops this type of alignment is still not understood. Also the possibility that a finite time singularity may develop is not ruled out by this analysis. As the paper of Constantin *et al.*<sup>24</sup> demonstrates for the quasigeostrophic equations, the question whether exponential growth or infinite growth in finite time occurs may depend critically on the choice of the initial conditions.

#### ACKNOWLEDGMENTS

We like to acknowledge discussions with H. Friedel and M. Berning and we thank K. H. Spatschek for his continuous support. This work was performed under the auspices of the Sonderforschungsbereich 191.

<sup>1</sup>U. Frisch and G. Parisi, in *Turbulence and Predictability in Geophysical Fluid Dynamics and Climate Dynamics*, edited by M. Ghil, R. Benzi, and

G. Parisi (North-Holland, New York, 1985), pp. 84–88.

<sup>2</sup>Z.-S. She and E. Leveque, Phys. Rev. Lett. **72**, 336 (1994).

<sup>3</sup>B. Dubrulle, Phys. Rev. Lett. **73**, 959 (1994).

<sup>4</sup>Z.-S. She and E. C. Waymire, Phys. Rev. Lett. **74**, 262 (1995).

<sup>5</sup>R. Grauer, J. Krug, and C. Marliani, Phys. Lett. A **195**, 335 (1994).

<sup>6</sup>H. Politano and A. Pouquet, Phys. Plasmas **2**, 2931 (1995).

<sup>7</sup>J. Herweijer and W. van de Water, Phys. Rev. Lett. **74**, 4651 (1995).

<sup>8</sup>S. Chen, K. R. Sreenivasan, M. Nelkin, and N. Cao, Phys. Rev. Lett. **79**, 2253 (1997).

<sup>9</sup>S. Grossmann, D. Lohse, and A. Reeh, Phys. Fluids **9**, 3817 (1997).

<sup>10</sup>V. Gurarie and A. Migdal, Phys. Rev. E **54**, 4908 (1996).

<sup>11</sup>E. Balkovsky, G. Falkovich, I. Kolokolov, and V. Lebedev, Phys. Rev. Lett. **78**, 1452 (1997).

<sup>12</sup>P. Constantin, C. Fefferman, and A. J. Majda, Commun. Part. Diff. Eq. **21**, 559 (1996).

<sup>13</sup>A. Pouquet, in *Plasma Astrophysics*, No. 468 in Lecture Notes in Physics, edited by C. Chiuderi and G. Einaudi (Springer-Verlag, Berlin, 1996), pp. 163–212.

<sup>14</sup>P. L. Sulem, U. Frisch, A. Pouquet, and M. Meneguzzi, J. Plasma Phys. **33**, 191 (1985).

<sup>15</sup>M. J. Berger and P. Colella, J. Comput. **82**, 64 (1989).

<sup>16</sup>H. Friedel, R. Grauer, and C. Marliani, J. Comput. Phys. **134**, 190 (1997).

<sup>17</sup>J. B. Bell, P. Colella, and H. M. Glaz, J. Comput. Phys. **85**, 257 (1989).

<sup>18</sup>J. B. Bell and D. L. Marcus, J. Comput. Phys. **101**, 334 (1992).

<sup>19</sup>R. Grauer and C. Marliani, Phys. Plasmas **2**, 41 (1995).

<sup>20</sup>U. Frisch, A. Pouquet, P. L. Sulem, and M. Meneguzzi, J. Méc. Théor. Appl. **Numéro spécial**, 191 (1983).

<sup>21</sup>D. Biskamp and H. Welter, Phys. Fluids B **1**, 1964 (1989).

<sup>22</sup>R. Kinney, T. Tajima, J. C. McWilliams, and N. Petviashvili, Phys. Plasmas **1**, 260 (1994).

<sup>23</sup>R. Kinney, J. C. McWilliams, and T. Tajima, Phys. Plasmas **2**, 3623 (1995).

<sup>24</sup>P. Constantin, A. J. Majda, and E. G. Tabak, Phys. Fluids **6**, 9 (1994).